Engineered Science
DOI: https://dx.doi.org/10.30919/es1064

Deep Neural Network as a Tool to Classify and Identify the 316L SS And AZ31BMg Metal Surface Morphology: An Empirical Study

Pushpanjali Bhat,[1,#] Tanmay Shukla,[2,#] Nithesh Naik,[3] Daniel Korir,[4] Princy Randhawa,[5] Antony V Samrot,[6] Ramya S[7,*] and Salmataj S A[8,*]

Abstract

Identifying the severity of corrosion is crucial in physical and biological sciences. Developing a highly accurate deep learning model capable of classifying corrosion severity across a wide metal surface, even with limited training data, represents a significant advancement over traditional investigation methods. Unlike traditional approaches such as electrochemical measurements that assess only provided inspection areas, deep learning models can classify the entire metal surface. In the realm of biomaterials, this corrosion identification approach aids researchers in selecting appropriate materials for body implants, reducing the impact of corroded metal reactions within the implanted body. This research advocates for an objective and automated examination of metal surfaces, employing convolutional neural networks to classify corrosion intensity based on scanning electron microscope (SEM) images. Despite the limited number of samples from electrochemical laboratories, the deep learning model provides valuable insights across the entire metal plate surface, effectively distinguishing between different corrosion states. Electrochemical measurements were implemented to see the corrosion such as electrochemical impedance spectroscopy (EIS), potentiodynamic polarisation (PDP) techniques. Generative Adversarial Network (GAN) is implemented to generate synthetic images. SEM images were obtained to evaluate the changes at microlevel and CNN was used to classify the images with an efficiency of 92.7%.

Keywords: EIS; Nyquist plot; CNN; GAN; Corrosion.
Received: 22 November 2023; Revised: 16 December 2023; Accepted: 18 December 2023.
Article type: Research article.

1. Introduction

Metals and alloys are integral components in various global industries, including construction, oil and gas, and manufacturing. Essential materials like steel, magnesium, cobalt, platinum, and steel alloys find extensive use as biomaterials for body implants.[1] Despite their widespread application, metal surfaces are susceptible to corrosion when exposed to atmospheric conditions. In industrial settings, corrosion poses a significant threat, and early detection is crucial for risk mitigation and the implementation of safety measures.[2]

The use of biomaterials in human body implants introduces an additional challenge as these materials are consistently exposed to physiological mediums, influencing their corrosion behavior. Corrosion on biomaterials implanted in the human body can have severe consequences, including life-threatening complications and potential fatalities. Therefore, extensive research is essential for selecting appropriate biomaterials and understanding their interactions with the surrounding physiological environment before they are employed for implantation.[1]

In the realm of biomaterials, it is imperative to subject

[1] *Department of Chemistry, Manipal Institute of Technology, Manipal Academy of Higher Education, Manipal, 576104, Karnataka, India.*
[2] *Department of Quantitative Biomedical Science, Dartmouth College, Hanover 03766, New Hampshire USA.*
[3] *Department of Mechanical and Industrial Engineering, Manipal Institute of Technology, Manipal Academy of Higher Education, Manipal 576104, Karnataka, India.*
[4] *Department of Chemistry and Biochemistry, East Texas Baptist University, Marshall Texas 75650 USA.*
[5] *Department of Mechatronics, Manipal University Jaipur, Jaipur 303007, Rajasthan, India.*

metallic alloys to thorough testing for their behavior in physiological mediums. The identification of corrosion through scanning electron microscopy (SEM) images of metal surfaces is a viable approach to assess the extent of corrosion.[2] Several classical methods exist for surface analysis, but they heavily rely on the expertise of the research analyst evaluating corrosion intensity. These classical methods can only predict and evaluate corrosion on the specific surface imaged under the microscope, lacking the generalizability to larger metal surfaces. This limitation underscores the need for skilled research analysts to meticulously select areas for corrosion assessment on metal surfaces.

In one study,[3] employed deep learning models to analyze microscopic images of corroded copper and steel laminas, investigating the effectiveness of inhibitor solutions in reducing corrosion. The study utilized metal coupons made of steel and copper to assess the impact of inhibitor solutions on corrosion levels. Microscopic images of these metal surfaces were captured at various time points, both with and without exposure to inhibitor solutions, and were subsequently analyzed. The dataset's limited size prompted the use of augmentation techniques[4] to increase the volume of available data. The current study focuses on identification and classification based on SEM images of metal coupons exposed to physiological medium.

2. Methodology

2.1 Materials

The investigation on corrosion involved the utilization of the Magnesium AZ31B alloy and 316L stainless steel alloys, and the detailed composition of these alloys are provided in Tables 1 and 2.

2.1.1 Test specimen preparation for Electrochemical measurements

A cylindrical rod, 50 mm in height and 5 mm in diameter, was cut from rods of magnesium AZ31B alloy and 316L Stainless steel alloy respectively. To create test coupons, these rods were moulded to a height of 30 mm using epoxy resin. The bottom surface, which remained un-moulded, were polished using sandpaper with varying grit sizes, ranging from 110 to 1600. A highly reflective mirror surface was achieved through the use of a disc polishing wheel and 1.0-micron alumina powder,

2.1.2 Electrochemical method

Electrochemical investigations were carried out using a CH potentiostat, the CHI604D series with β software, obtained from the United States. The potentiostat was linked to three electrodes: Magnesium AZ31B alloy or 316L Stainless steel alloy as the anode, a mercury mercurous chloride saturated electrode as the cathode, and inert platinum as the counter electrode. These electrodes were immersed in 100 ml of simulated physiological medium.

2.1.3 Potentiodynamic polarisation method (P.P.M.)

To produce the polarization curves for the oxidation of Magnesium AZ31B alloy or 316L stainless steel alloy and the reduction of H_3O^+, the anode was polarized at -250 mV in the cathodic direction and +250 mV in the anodic direction relative to the equilibrium state potential. This was accomplished at a sweep rate of 1 mV sec^{-1}.

2.1.4 Electrochemical impedance spectroscopy method (E.I.S.)

Electrochemical Impedance Spectroscopy (E.I.S.) experiments involved applying a 10 mV alternating current signal at the equilibrium potential and scanning frequencies from 100 kHz to 0.01 Hz. P.P.M. readings are taken after E.I.S. without further polishing the metal surface.

2.1.5 Test specimen preparation

Magnesium AZ31B alloy coupons and Stainless steel 316L alloy coupons were used for the experiments. Magnesium AZ31B alloy coupons were polished on grit paper of varying sizes 800 to 1200 and Stainless steel 316L coupons were polished on grit paper of varying sizes 200 to 1200 for smooth and mirror finishing. Mirror finishing was done so that at the micro-level the surface of the coupons was smooth hence corrosion due to uneven surface structure would be avoided hence providing precise results. The coupons were then cleansed with acetone to remove all the contaminants, prior to immersion. The coupons were immersed in 40 mL of simulated physiological medium.

2.1.6 Surface morphology studies (S.E.M.)

The surface characteristics of the Magnesium AZ31B alloy or 316L stainless steel alloy were investigated employing the

[6] *Faculty of Medicine, MAHSA University, 42610, Jenjarom Selangor, Malaysia.*
[7] *Department of Electronics and Communications Engineering, Manipal Institute of Technology, Manipal Academy of Higher Education, Manipal 576104, Karnataka, India.*
[8] *Department of Biotechnology, Manipal Institute of Technology, Manipal Academy of Higher Education, Manipal 576104, Karnataka, India.*
[#] *authors have contributed equally.*
**Email:* ramya.lokesh@manipal.edu (Ramya S), salma.taj@manipal.edu (S. Salmataj)

Table 1. Constituents of Magnesium AZ31B alloy.

Alloy name	Composition (%)							
AZ31B Magnesium alloy	Al	Zn	Mn	Si	Fe	Cu	Ni	Mg
	3.15	0.99	0.31	0.016	0.003	0.0026	0.0008	Bal

Table 2. Constiuents of the 316L stainless steel alloy.

Alloy name	Composition (%)						
	C	Si	Mn	P	S	Cr	Ni
316L Stainless steel	0.032	0.442	1.81	0.028	0.013	16.96	10.39
	Mo	Al	Cu	Co	As	Nb	V
	1.80	0.141	0.60	0.156	0.014	0.016	0.058
	W	Fe	Sn				
	0.025	67.5	0.012				

JEOL JSM-6380L Analytical scanning electron microscope. This examination involved immersing the test coupons in simulated physiological mediums, SEM, imaging was performed at 20 kV under high vacuum with objective aperture 10 µm and 20 µm. Hence obtained SEM images were used for further processing. Methodology adopted for the Texture based classification of corroded metallic surface is shown in Fig. 1. Original dataset is made up of microscopic images taken SEM electron microscope at 500x magnification and focal length of 10 micro meter, as these images are digitally generated so brightness and light exposure effects texture and contrast of image. Since number of samples were less, Generative Adversarial Network (GAN) is implemented to generate synthetic images. The images are validated and stored in the database. These Images are mainly classified based on type of metallic surface and extend of corrosion on them, for classification based type of metallic surface specific feature like strides on 316L Stainless Steel alloy and cloudy appearance on Magnesium AZ3B alloy are used as reference feature in the custom Convolution Neural Network (CNN) model.

2. Generative Adversarial Network (GAN) and custom image data generator

GANs[5] and Image generator algorithms were used to generate the synthetics images as a limited dataset was available. Fig. 2 shows the GAN architecture to generate synthetic SEM images. In GAN, a generator network is used to generate synthetic images along with an image augmenter and a discriminator network is used to provide backward feedback to tune the model and increase its accuracy. The generator network consists of a five-layer network with leaky ReLU as an activation function and batch normalization as an optimizing technique.

A generative adversarial network (GAN) has two parts. Fig. 3 shows the individual architecture of generator and discriminator of GAN. The generator learns to generate plausible data. The generated instances become negative training examples for the discriminator. The generator part of a GAN learns to create fake data by incorporating feedback from the discriminator. It learns to make the discriminator classify its output as real. Generator training requires tighter integration between the generator and the discriminator than discriminator training requires.

The discriminator learns to distinguish the generator's fake data from real data. The discriminator penalizes the generator for producing implausible results. The discriminator in a GAN is simply a classifier. It tries to distinguish real data from the data created by the generator. It could use any network architecture appropriate to the type of data it's classifying.

Both the generator and the discriminator are neural networks. The generator output is connected directly to the discriminator input. Through backpropagation, the discriminator's classification provides a signal that the

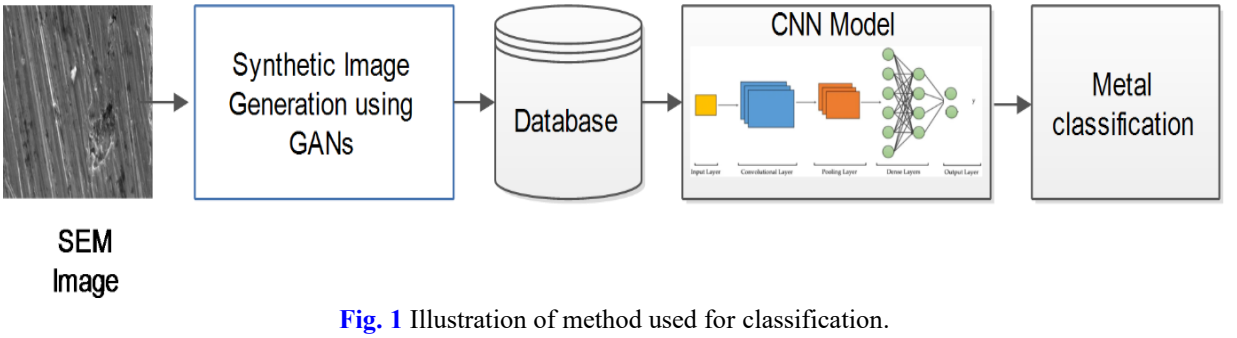

Fig. 1 Illustration of method used for classification.

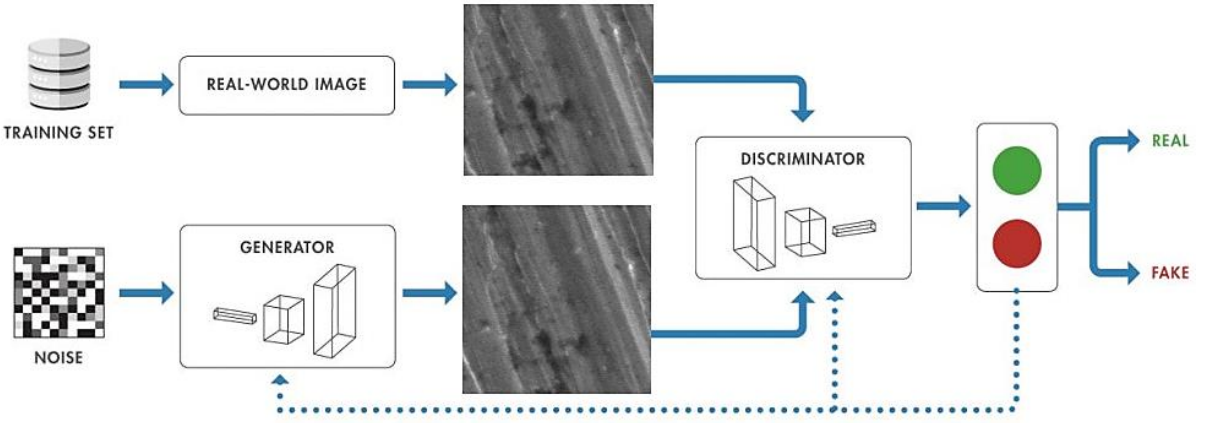

Fig. 2 Block diagram of Synthetics image generator using GAN.

generator uses to update its weight.

Vanishing Gradient Problem is observed when higher the complexity of input data, more the number of layers needed to fit its complexity hence more activation functions over the neural net causing gradients of loss function approach zero to alleviate this problem use of ReLU is advised.

Constraints-

1) Appearance (Intensity and Gradient)-

Intensity penalty guarantees the similarity of all pixels in Greyscale space. Gradient penalty can sharpen the generated images. For intensity L2 distance between predicted frame *I'* and ground truth I is minimized as:

$$L_{int}(\hat{I}, I) = \left|\left|\hat{I} - I\right|\right|_2 \quad (1)$$

2) Gradient loss

For gradient loss, Temporal loss is defined as the difference between the optical flow of prediction frames and ground truth as shown in equation 2.

$$L_{gd}(\hat{I} - I) = \sum \left|\left||\hat{I}_{i,j} - \hat{I}_{i-1,j}| - |I_{i,j} - I_{i-1,j}|\right|\right|_1 + \left|\left||\hat{I}_{i,j} - \hat{I}_{i,j-1}| - |I_{i,j} - I_{i-1,j}|\right|\right|_1 \quad (2)$$

$$L_{op} = ||f(\hat{I}_{t+1}, I_t) - f(I_{t+1}, I_t)||_1 \quad (3)$$

3) Predictor (Least Square GAN) -

A GAN contains a discriminative network D, and a generator network G. G learns to generate frames that are hard to be classified by D, while D aims to discriminate the frames generated by G. U-Net is treated as the Generator in this paper. For Discriminator, a patch discriminator which means each output scalar of D corresponds to a patch of an input image.

Algorithm-

D has to classify I_{t+1} (observed/ground truth) into class 1 - genuine label and I'_{t+1} (Generated/predicted) into class 0 - fake label.

To train D we fix weights of G, MSE is used:

$$L_{adv}^{D}(\hat{I}, I) = \sum \frac{1}{2} L_{MSE}(D(I)_{i,j}, 1) + \sum \frac{1}{2} L_{MSE}\left(D(\hat{I})_{i,j}, 0\right) \quad (4)$$

(i, j) are spatial patch indices.

Here L_{MSE} is:

$$L_{MSE}(\hat{Y}, Y) = (\hat{Y} - Y)^2 \quad (5)$$

To train G we fix weights of D, and such that D classifies those generated frames into class 1, similarly an MSE function is used:

$$L_{adv}^{G}(\hat{I}) = \sum_{i,j} \frac{1}{2} L_{MSE}\left(D(\hat{I})_{i,j}, 1\right) \quad (6)$$

These Constraints are then combined to obtain an Objective function which is:

$$L_G = \lambda_{int} L_{int}(\hat{I}_{t+1}, I_{t+1}) + \lambda_{gd} L_{gd}(\hat{I}_{t+1}, I_{t+1}) + \lambda_{op} L_{op} + \lambda_{adv} L_{adv}^{G}(\hat{I}_{t+1}) \quad (7)$$

The discriminator is trained using the following loss function-

$$L_D = L_{adv}^{D}(\hat{I}_{t+1}, I_{t+1}) \quad (8)$$

Implementation details:

- Intensity of pixels in all frames are normalized to [-1, 1].
- Size of each frame is resized to 450 × 450.
- t = 4 and uses a random clip of 5 sequential frames.
- Mini-batch size is 4.
- For grayscale, the learning rate of the Generator and Discriminator is set to 0.0001 and 0.00001.

Coefficients are set accordingly for each segment of the algorithm.

In the Custom image generator algorithm, various image augmentation techniques were used to expand the size of the dataset. In Image augmentation, different transformations are applied to original images which results in multiple transformed copies of the same image. Each generated copy is different from the other in certain aspects depending on the

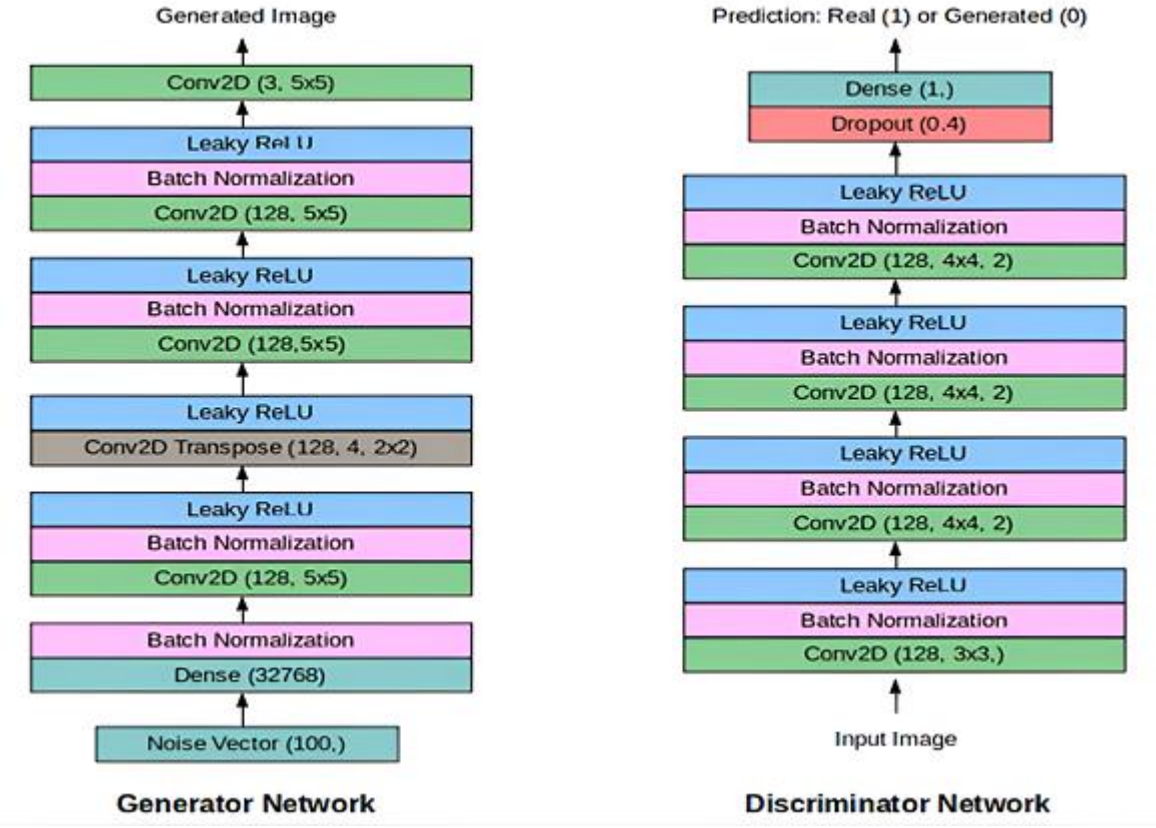

Fig. 3 Details of GAN model architecture.

augmentation techniques applied like shifting, rotating, flipping, *etc*. these small amounts of variations that are applied on the original image does not change its target class but only provides a new perspective of capturing essential features. These image augmentation techniques not only expand the size of dataset but also incorporate a level of variation in the dataset which allows your model to generalize better on unseen data. This algorithm helps the model to becomes more robust when it is trained on new and slightly altered images. Image Data Generator class ensures that the model receives new variations of the images at each epoch. But it only returns the transformed images and does not add it to the original corpus of images. In fact, it prevents the case of overfitting in our model as the number of images in our dataset are limited. Another advantage of Image Data Generator is that it requires lower memory usage. This is so because without using this class, we load all the images at once. But on using it, we are loading the images in batches which saves a lot of memory.

Various techniques used in Image Data generator are as follows:

Random Flips – In Image Data Generator class were randomly rotated through any degree between 0 and 360.

Random Rotation - It may happen that the object may not always be in the centre of the image. To overcome this problem, we can shift the pixels of the image either horizontally or vertically; this was done by adding a certain constant value to all the pixels.

Random Shift - Flipping images is also a great augmentation technique and it makes sense to use it with a lot of different objects. Image Data Generator class has parameters horizontal flip and vertical flip for flipping along the vertical or the horizontal axis.

Random Brightness - It randomly changes the brightness of the image. It is also a very useful augmentation technique because most of the time our images were not be under perfect lighting condition. So, it becomes imperative to train our model on images under different lighting conditions.

Random Zoom - The zoom augmentation either randomly zooms in on the image or zooms out of the image.

The Generator's final output is a synthetic image, ostensibly indistinguishable from real SEM images, ready for validation and training in the CNN. The synthetic images generated by the GAN are undergo a validation process where both their individual quality and collective diversity are assessed.

Internal GAN Validation: Within the GAN framework, the Discriminator's ability to distinguish real from synthetic images serves as the first level of validation. As the training progresses and the Generator improves, the Discriminator's classification accuracy becomes a metric of the synthetic

images' quality.

External Validation: Beyond the GAN's internal metrics, additional external validation techniques are applied. These might include structural similarity indices, L2 norms for intensity consistency, and gradient checks to ensure the synthetic images are not just plausible but also maintain the textural and morphological characteristics essential to SEM imagery.

Temporal Consistency Checks: Temporal loss functions are utilized to compare the optical flow of consecutive frames, ensuring that the synthetic images possess temporal coherence when representing dynamic processes, a critical aspect when real SEM imagery might include time-lapse or sequential imaging. Few images are distorted, hence are removed from the dataset as it may affect the training of the deep neural network. Table 3 shows the dataset details.[6]

3. Results and discussion

3.1 Electrochemical measurements

The electrochemical measurement are studied to understand the effect of physiological medium on 316L stainless steel alloy and AZ31B Magnesium alloy.

3.1.1 Potentiodynamic polarization (PDP) technique

Figures 4 (a) and (b) shows the potentiodynamic polarization plot for the corrosion of 316L stainless steel and Magnesium AZ31B alloy in simulated physiological medium at a different temperature.

Different potentiodynamic polarization parameters like, corrosion potential ($E_{corr.}$), corrosion current density ($i_{corr.}$), cathodic Tafel slope ($-\beta_c$) and anodic Tafel slope (β_a) were obtained from the potentiodynamic polarization plots[7].

Results of the potentiodynamic polarization measurements[8] for the corrosion of 316L stainless steel alloy and Magnesium AZ 31B alloy in simulated physiological medium are given in Table 4.

Table 3. Details of dataset used for the classification.

S. No	SEM images containing Corrosion on Metallic surface	No. of original Images	No. of valid synthetic Images Generated
1	316L Stainless Steel alloy	12	77
2	Magnesium AZ31B alloy	13	108

Table 4. Potentiodynamic polarization measurements for the corrosion of 316L stainless steel alloy and AZ31B Magnesium alloy in simulated physiological medium.

Name of alloy	Temp. (K)	$i_{corr.}$ ($\times 10^{-5}$A cm^{-2})	C.R. (mm y^{-1})	β_a (V dec^{-1})	$-\beta_c$ (V dec^{-1})	$E_{corr.}$ (mV vs SCE)
316L Stainless steel alloy	303	7.203	28.14	1356.5	1098.8	-413.0
	313	7.834	30.61	1601.3	916.6	-371.0
	323	9.647	37.69	1190.7	837.5	-375.0
AZ31B Mg alloy	303	5.420	6.581	427.7	542.6	-1542
	313	7.466	9.065	451.4	541.6	-1549
	323	9.611	11.67	419.4	531.4	-1533

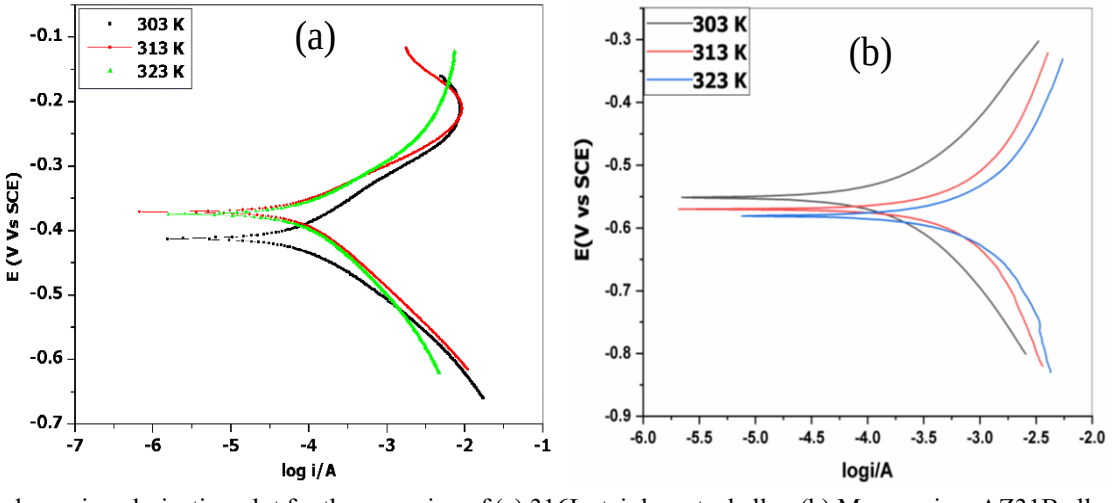

Fig. 4 Potentiodynamic polarization plot for the corrosion of (a) 316L stainless steel alloy (b) Maganesium AZ31B alloy at a different temperaturses.

From the results obtained from the Potentiodynmic polarization method, it is observed that equilibrium corrosion potential values obtained for both metals are nearer to their equilibrium corrosion potential when exposed to aqueous solution (500 mV for Stainless steel and 1500 mV for Magnesium). This shows that both metals undergo corrosion when exposed to a simulated physiological medium.

The effect of simulated physiological medium to both metals are also studied by change of temperature as in body there will be change of temperature takes place due to different physiological actions. It is observed that there will be increase in corrosion current density (A cm^{-2}) and corrosion rate with increase in temperature. This indicates that 316L stainless steel or Magnesium AZ31B alloy dissolution increases with the temperature.

The parallel anodic and cathodic polarization curves suggest that the both metal dissolution and hydrogen evolution are activation controlled, and the mechanism of both anodic and cathodic reactions are not affected by the change of temperature.[7] There is no much change in the values of anodic tafel and cathodic tafel slope. This indicates that the change of temperature is not affecting the mechanism and may change the kinetics of both anodic and cathodic reactions.

According to a study,[8] if the displacement in corrosion potential is less than ± 85 mV then both the reactions are equally affected by the change of temperature. In the present study, there is no observable shift in corrosion potential ($E_{corr.}$) on change of temperature suggesting that the both the reactions are equally affected by the increase of temperature. There is slightly positive shift in corrosion potential may be due to the anodic reaction is more affected than the cathodic reaction by the increase of temperature.

3.1.2 Electrochemical impedance spectroscopy (EIS) studies

In order to gain more information about the corrosion, electrochemical impedance spectroscopy measurements[12] were carried out for the 316L Stainless steel or AZ31B Magnesium alloy in simulated physiological medium at different temperatures. Figs. 5(a) and (b) represent Nyquist plot of 316L stainless steel or AZ31B Magnesium alloy in simulated physiological medium at different temperatures.

As can be seen from Figs. 5(a) and (b) the impedance diagrams show semicircles, indicating that the corrosion process is mainly charge transfer controlled. The diameter of the semicircle gives the charge transfer resistance.[9] The charge transfer resistance, double layer capacitance obtained for 316L stainless steel and AZ31B magnesium alloys are nearer to the values when these metals are exposed to aqueous solutions. These confirms the corrosion of these metals in simulated physiological medium.

As the temperature increases there will be decrease in the diameter. This indicates that charge transfer at the metal solution interface increases with increase of temperature.

In AZ31B Magnesium alloy at a frequency nearer to 100000 Hz, a capacitive loop develops due to the movement of ions involved during magnesium oxidation, H^+ reduction, and inert magnesium oxide film development.[10] The MgO film allows the movement of ions and possesses dielectric properties. Hence film can be assumed to be a circuit having a resistor and capacitor. The capacitive curve recorded at a frequency nearer to 100 kHz is significant in intermediate steps. The net result of intermediate steps is the conversion of Magnesium to Mg^{2+} at the two margins. First oxidation at magnesium AZ31B alloy is in contact with MgO. The second oxidation to Mg^{2+} at MgO is in contact with physiological medium and the formation of OH^- or O^{2-} from H_2O. Among these intermediate steps, all the steps may overlap, or one step

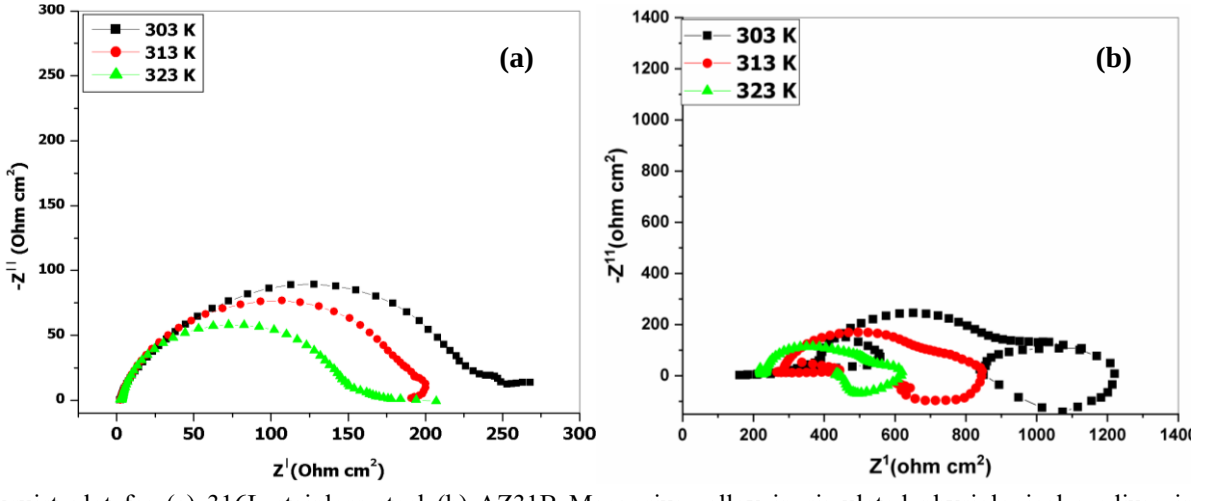

Fig. 5 Nyquist plot for (a) 316L stainless steel (b) AZ31B Magnesium alloy in simulated physiological medium in different temperatures.

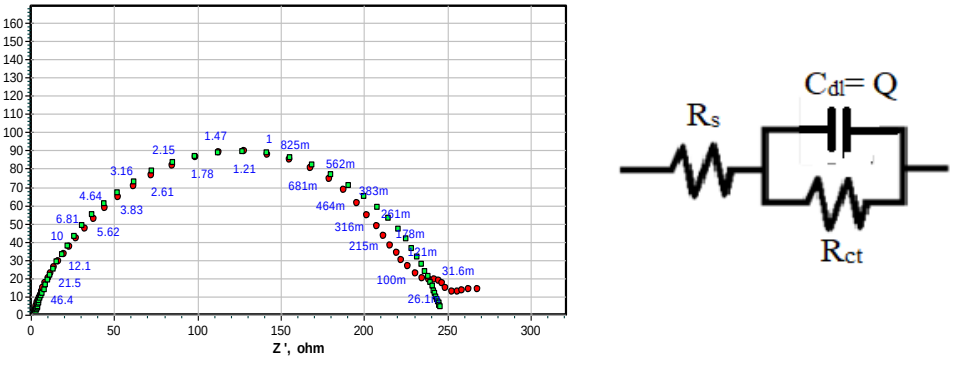

Fig. 6 (a) Stimulated circuit fitted to the obtained EIS data b) Circuit used to fit the experimental EIS data for 316L stainless steel in simulated physiological medium at 313 K.

may take place majorly to give the half-circle shaped capacitive curve.[11-13] The diameter of this loop is considered as charge transfer resistance (R_{ct}).

The frequency closer to 0.01 Hz the inductive curve was found as a result of the relaxation of charged ions gained by adsorption and movement on and into the MgO film.

Analysis of Nyquist plot can be done by fitting the impedance data to suitable equivalent circuit by software ZSimpWin (3.21). The impedance fit and the equivalent circuit are given in Figs. 6 and 7. The impedance parameters obtained by fitting the data into equivalent circuit are given in Table 5.

In Fig. 6(b) R_S is charge transfer resistance, C_{dl} is double layer capacitance at the interface between the metal and solution. R_{ct} is Charge transfer resistance. In circuit 7(b) R_s resistance of solution present between the electrodes, R_L. inductive resistance, L inductance, Q constant phase element, C_1, R_1 capacitance, and resistance at Magnesium and MgO boundary, C_2, R_2 capacitance and resistance at MgO and physiological medium boundary.

From the impedance parameters it is observed that as the temperature increases there will be decrease in the polarization resistance and increase in the double layer capacitance. This may be due to with increase of temperature; there will be increase in the metal dissolution and increase in the conductivity of medium. This decreases the thickness of the double layer.[13-15]

4. Deep neural networking studies

4.1 Architecture development

Many researchers[16-18] explored the texture based classification on the metallic surface. The proposed work explored many pre-trained models like VGG-16,[19] VGG-19,[20] YoLo,[21] *etc*. It was concluded that it is a difficult task to implement models based on transfer learning for the binary classification of given images as they are trained on daily life objects, and our data is based on images that taken from a scanning electron microscope. Also, our dataset is made up of grey scale images thus the pre-trained models with adjustable weights are incompatible, as they require colour and gradient change for proper texture detection of surface and accuracy obtained was below 30 %. Various open-source CNN[22] models were implemented, but they failed to classify images into proper classes and the accuracy that was obtained is below 45%. Thus, a custom-designed 8-layered CNN model is used with various custom filter inspired by the architecture of the visual geometry group, and achieved an accuracy of 92.4 % with just 400 Epochs of training.

Table 5. Impendence parameters for corrosion of 316L stainless steel and AZ31B magnesium alloy in simulated physiological medium.

Name of Alloy	Temperature (K)	C_{dl} ($\times 10^{-4}$ F cm^{-2})	R_P (ohm cm^2)
316L Stainless Steel	303	1.931	318.9
	313	4.5637	246.839
	323	5.3313	196.019
AZ 31BMagnesium alloy	303	6.11	1056.81
	313	11.23	938.52
	323	15.48	794.80

4.2 CNN custom model

This model classify images in 316L Stainless Steel and Magnesium AZ31B category and label them. The CNN model[23] is trained on original and generated dataset using GANs and Image generator Algorithm. The input shape of channel training data is (450, 450, 3). The CNN architecture consists of 5 convolutional layers, 4 dense layer, ReLU activation function in convolutional and hidden layers, 5 Batch-Normalization and 4 Max-pooling layers between every convolutional layer, Dropout function is attached after every

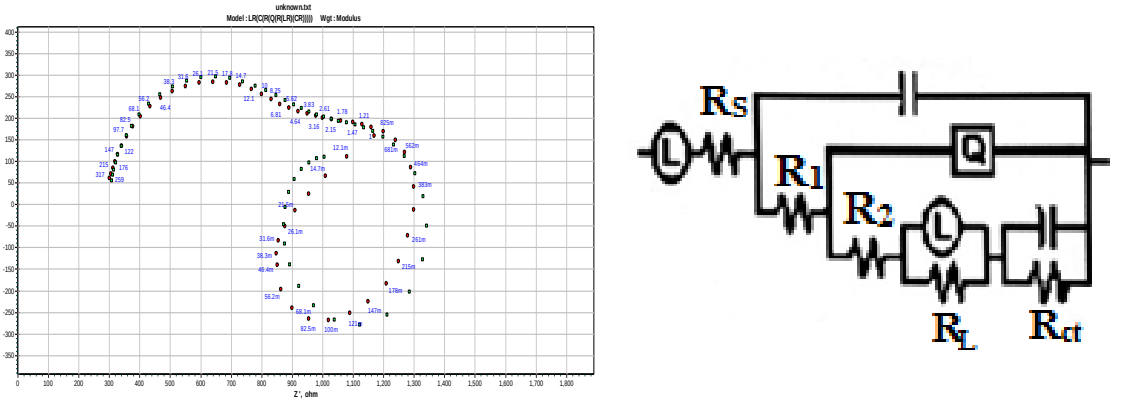

(a) (b)

Fig. 7 (a) Stimulated circuit fitted to the obtained EIS data b) Circuit used to fit the experimental EIS data for Magnesium AZ31B alloy in simulated physiological medium at 313 K.

batch of convolution layers, learning rate of 0.0007 and Adam optimiser over binary cross entropy loss function. This custom CNN model focuses on detection of certain pattern for classification of images like it looks for cloudy like pattern and texture in Magnesium AZ31B images and for 316L Stainless Steel in focuses on detection of stride like pattern on surface. The output of the models were concatenated and fed into a 4 layer neural network with 1 hidden layer. Sigmoid activation was used in the output layer with 4096 neurons. The architecture is as shown in Fig. 8.

4.3 Custom Filters for CNN Visualization

Due to limited availability of dataset, various methods were used to avoid overfitting and to increase accuracy by provide proper feedback to the neural network and adjusting its weight. One of major problem that faced was a sudden drop in accuracy after 200 Epocs of training and even changing various hyperparameters this problem persisted, so in order to avoid this problem we designed various custom filters that helps to visualize each and every layer of CNN model and gives output after every end of convolutional layer.

Figure 9 shows the visualization at 3,5,7,8,1 and 4th layer of CNN model using blue, RGB, aqua, moonlight, bronze, red lava and bone filter. These visualizations guide researchers in tweaking internal settings, ensuring the CNN focuses on relevant corrosion indicators.

Each filter serves a distinct purpose:

Blue_RGB Filter: Enhances contrast for better identification of subtle patterns, useful for detecting early signs of corrosion.

Aqua Filter: Shifts the color spectrum to reveal finer textural details, crucial for recognizing advanced corrosion with pronounced textures.

Moonlight Filter: Simulates a cooler color temperature, accentuating topographical variations caused by corrosion.

Bronze Filter: Detects warmth, potentially correlating with rust and warmer corrosion products.

Red Lava Filter: Emphasizes color intensity in areas with severe corrosion and significant oxidation.

Bone Filter: Renders images in high-contrast black and white, effectively isolating corroded and non-corroded areas.

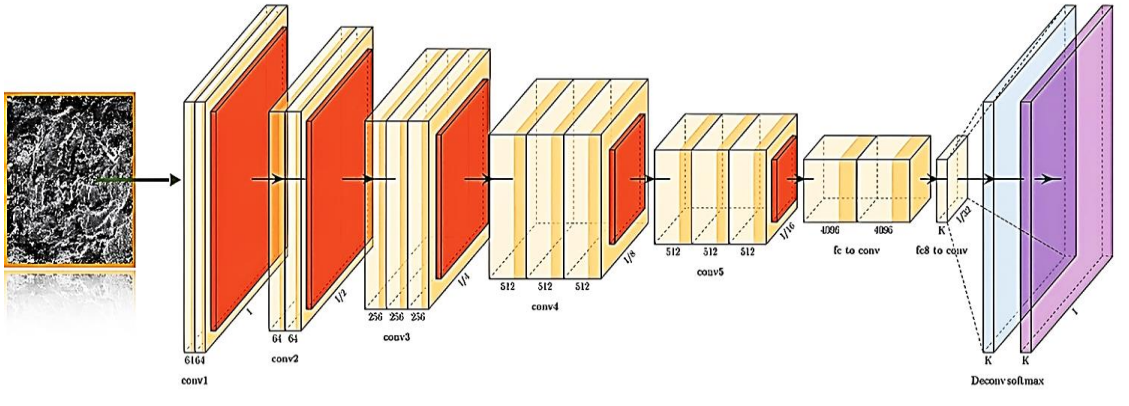

Fig. 8 Custom CNN model architecture.

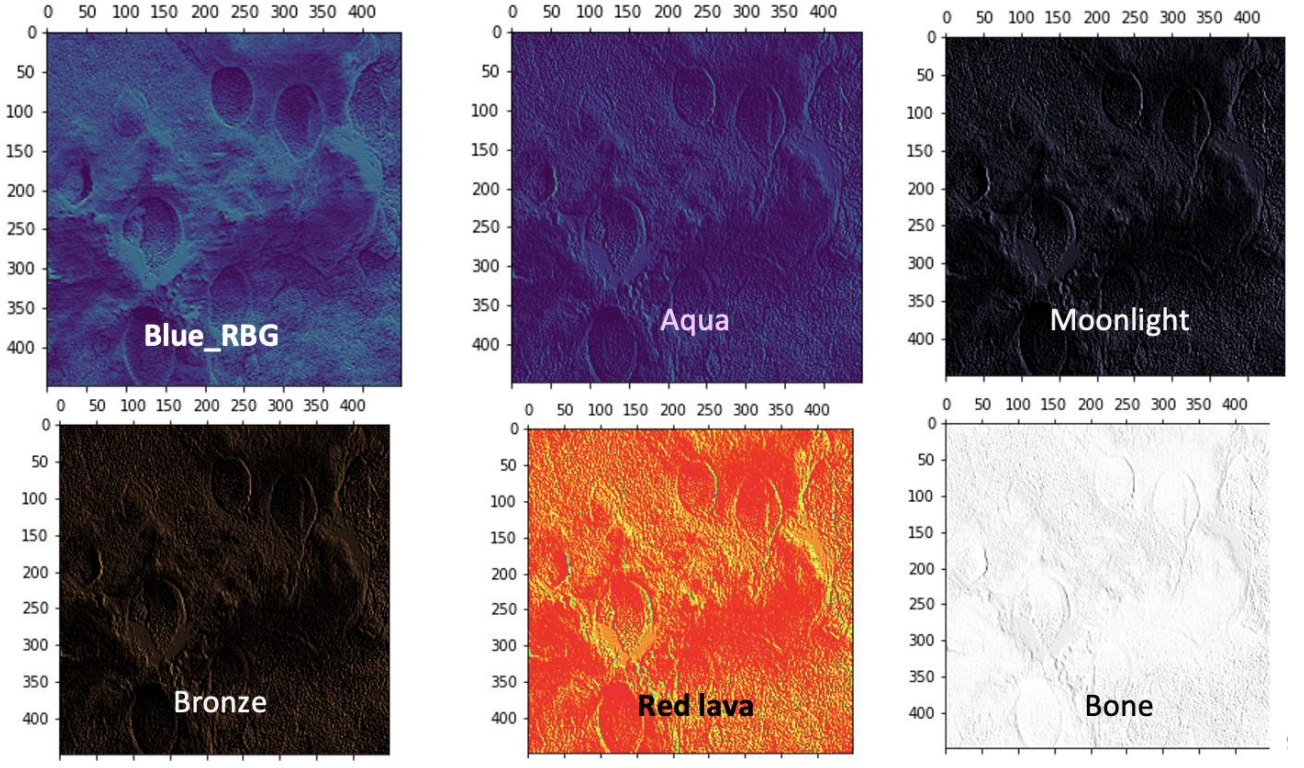

Fig. 9 Visualization of CNN layers with various filter (a) Blue_RBG (b) aqua (c) moonlight (d) bronze (e) red lava (f) bone filter.

4.4 Synthetic image generation using GAN

As the original SEM images are limited in number, GAN networks and Custom image Generator are used to increase the number of images by synthetically generation method. Fig. 10 shows the samples of original and synthetic images.

4.5 Training and Testing of CNN Model

Figures 11 and 12 depicts the validation accuracy and losses of the 8-Layer Custom CNN model used for binary classification of metallic surface into 316L Stainless Steel and Magnesium AZ31B. This CNN architecture uses 5 convolutional layers, 4 dense layer, multiple ReLU activation function in convolutional and hidden layers, 5 Batch-Normalization and 4 Max-pooling layers between every convolutional layer.

The CNN model has Total params: 3,453,121 and

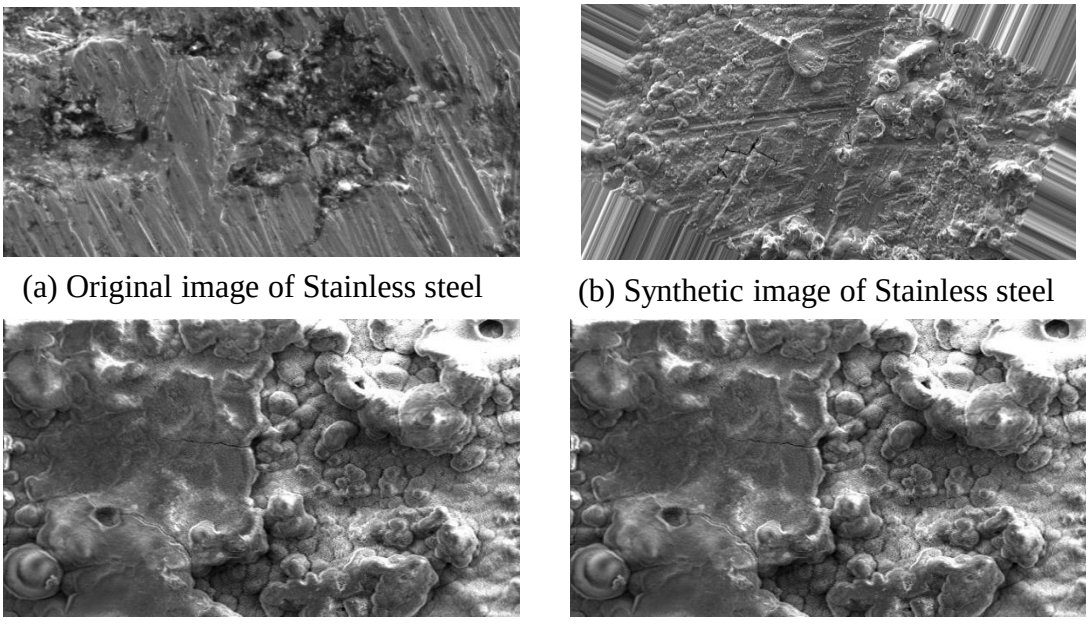

(a) Original image of Stainless steel (b) Synthetic image of Stainless steel

(c) Original image of Magnesium (d) Synthetic image of Magnesium

Fig. 10 Results of synthetic image generation using GAN.

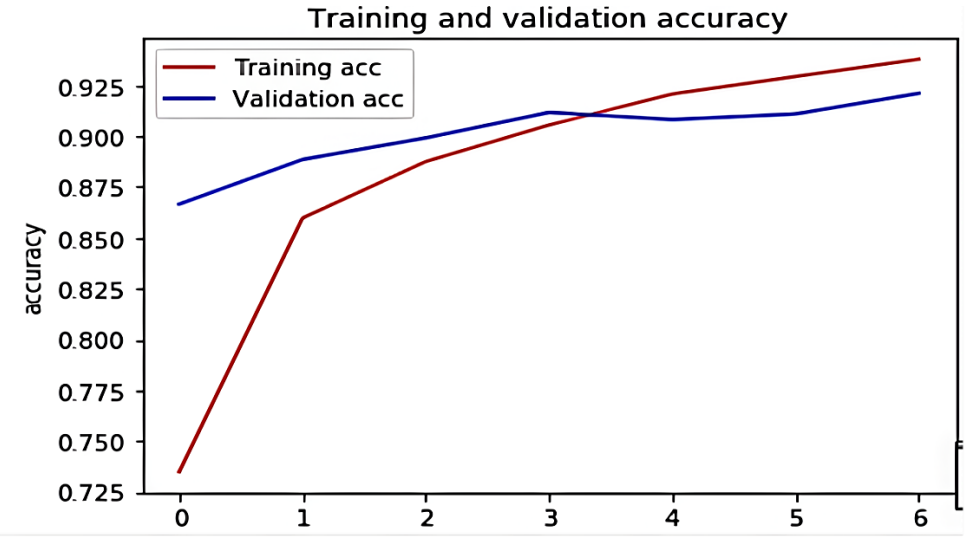

Fig. 11 Accuracy Plot of CNN model.

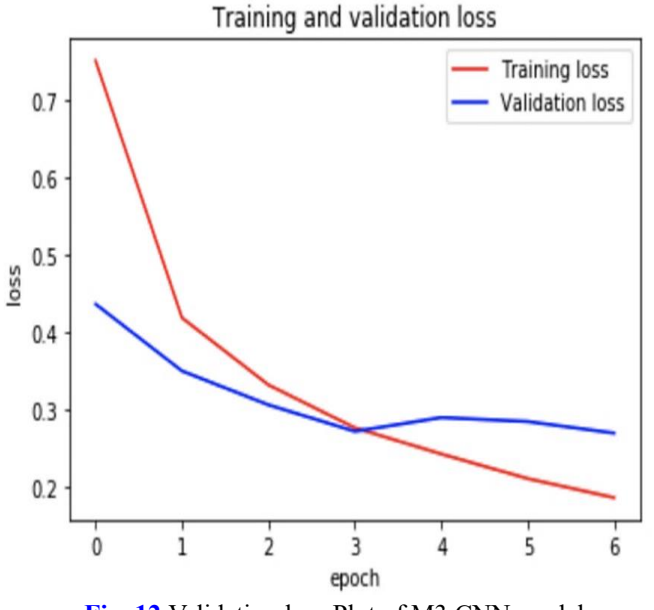

Fig. 12 Validation loss Plot of M3 CNN model.

Trainable params: 3,453,121. Thus Model summary of master CNN model has 603983872 weights in dense layers and 1204892 weights in convolutional layers as listed in Table 6. The input shape of training data's channel is (450,450 3) and output of the models were concatenated and fed into a 4 layers neural network with one hidden layer. Sigmoid activation was used in the output layer with 4096 neurons.

Validation accuracy[24] drops from 92% to 73% after 150 Epochs due improper positioning of Convolution layers, dense layers and visualisation of images, this problem was solved by using custom visualisation filters and libraries to adjusts the weights of respective layers.

After generating image of all layer's visualization, we were able to eliminate the problem and these visualizations also helped in identifying the misclassified data and according to those images weights of the models were adjusted and accuracy was improved by 4.7%. After implementing multiple techniques of classical machine learning models, it was decided that Deep learning will be used to solve this problem, where we have achieved an accuracy of 92.4%. We have

Table 6. CNN model summary.

Layer (type)	Output Shape	Param #
conv2d_8 (Conv2D)	(None, 148, 148, 32)	896
max_pooling2d_8 (MaxPooling2	(None, 74, 74, 32)	0
conv2d 9 (Conv2D)	(None, 72, 72, 64)	18496
max_pooling2d_9 (MaxPooling2	(None, 36, 36, 64)	0
conv2d_10 (Conv2D)	(None, 34, 34, 128)	73856
max_pooling2d_10 (MaxPooling	(None, 17, 17, 128)	0
conv2d_11 (Conv2D)	(None, 15, 15, 128)	147584
max_pooling2d_11 (MaxPooling	(None, 7, 7, 128)	0
flatten 2 (Flatten)	(None, 6272)	0
dense 4 (Dense)	(None, 512)	3211776
dropout 2 (Dropout)	(None, 512)	0
dense 5 (Dense)	(None, 1)	513

explored many optimizers as well as loss functions[25] and finally stuck to Adam and Binary Cross Entropy.[26]

4.4 Discussion on GAN and CNN architecture in classifying the metallic surface

The Generative Adversarial Network (GAN) framework significantly augments our limited SEM image dataset by refining the Generator's ability to create images indistinguishable from authentic SEM captures. Integrated into the CNN training pipeline, GAN-generated images enhance the model's understanding of real-world data variability, ensuring accuracy, robustness, and adaptability in material science applications.

The CNN model, tailored for metal surface classification, leverages hierarchical layers to detect specific corrosion patterns. For 316L stainless steel, it identifies 'stride patterns,' linear marks indicating corrosion, while for magnesium AZ31B, it recognizes 'blob and cloudy patterns' associated with pitting corrosion. Custom filters applied to CNN layers produce visualizations guiding adjustments, resulting in a 4.7% increase in accuracy (Figs. 13 and 14).

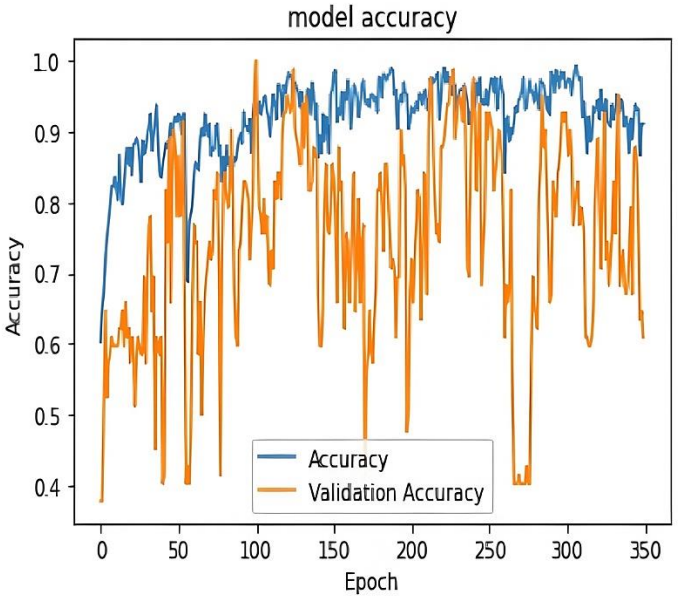

Fig. 13 Final CNN model accuracy.

Despite these advancements, applying deep learning models to corrosion detection using SEM images poses challenges, including the need for large, diverse datasets. The dynamic nature of corrosion requires consideration, and interpreting model decisions remains crucial. Our study addresses these challenges through rigorous strategies, such as data augmentation, regularization, hyperparameter optimization, and visualization-guided adjustments, showcasing deep learning efficacy in material science applications.

Holistic corrosion prediction integrates deep learning with advanced imaging, ensuring accuracy. Model adaptability is enhanced through domain adaptation and transfer learning. Dynamic parameter adjustment maintains long-term accuracy. Advanced feature engineering with deep networks enables detailed corrosion pattern identification. Hybrid modeling through data fusion improves predictive capabilities. Explainable AI fosters trust by providing insights. Real-time analysis via edge computing advances preventive maintenance. Deep learning accelerates material discovery for corrosion-resistant materials. Model robustness is heightened through advanced techniques, and automated data labelling streamlines manual efforts.

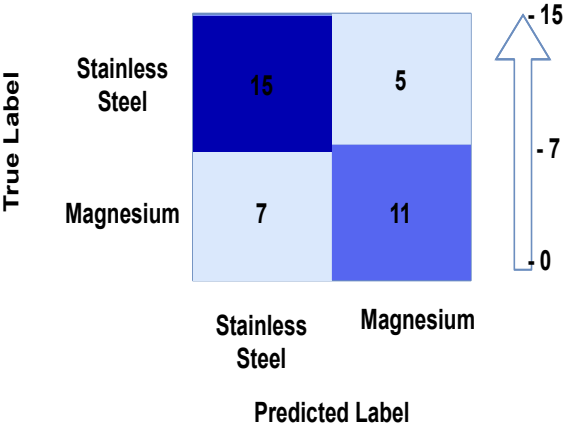

Fig. 14 Confusion matrix for CNN model.

5. Conclusion

Limited work has been done on applying deep learning techniques to microscopic images of corroded samples to predict the severity of metal corrosion. Unlike classical approaches limited to examining the surface under a microscope, deep learning models can extend the examination to the entire metal surface for identifying corrosion severity. Analyzing microscopic images provides insights into the microstructural features of the corroded metal surface, aiding in early-stage corrosion identification on surfaces not easily discernible with regular images.

The study investigates the application of GAN networks to generate synthetic SEM images, validated through electrochemical experiments. Surface morphological changes were observed using SEM. Utilizing transfer learning in deep neural networks for SEM images achieved a noteworthy recognition accuracy of 92.4%. The optimization of hyperparameters and weights in a Convolutional Neural Network (CNN) is a meticulous process, and visualizations from custom filters play a crucial role. These visual insights

create a feedback loop guiding strategic adjustments to the network's internal settings, resulting in a 4.7% improvement in accuracy by addressing misclassification issues.

Presently, the majority of artificial neural network (ANN) models applied for signal-to-noise improvements focus on reducing statistical noise in images. Advances in electron microscopy have enabled the correction of scan distortions and specimen drift. However, there is potential for additional deep learning models designed to address noise in images from optical microscopy and photoacoustic aberrations.

Acknowledgements

Authors are grateful to MAHE for the facilities provided. Authors also acknowledge MAHE seed money grant MAHE/0169/2019 received.

Conflict of Interest

There is no conflict of interest.

Supporting Information

Not applicable.

References

[1] N. Eliaz, Corrosion of metallic biomaterials: a review, *Materials*, 2019, **12**, 407, doi: 10.3390/ma12030407.

[2] B. T. Bastian, N. Jaspreeth, S. K. Ranjith, C. V. Jiji, Visual inspection and characterization of external corrosion in pipelines using deep neural network, *NDT & E International*, 2019, **107**, 102134, doi: 10.1016/j.ndteint.2019.102134.

[3] R. Stoean, C. Stoean, A. Samide, Deep learning for metal corrosion control: can convolutional neural networks measure inhibitor efficiency? 2018 20th International Symposium on Symbolic and Numeric Algorithms for Scientific Computing (SYNASC). September 20-23, 2018, Timisoara, Romania. IEEE, 2019, 387-393, doi: 10.1109/SYNASC.2018.00065.

[4] C. Shorten, T. M. Khoshgoftaar, A survey on image data augmentation for deep learning, *Journal of Big Data*, 2019, **6**, 1-48, doi: 10.1186/s40537-019-0197-0.

[5] L. Lan, L. You, Z. Zhang, Z. Fan, W. Zhao, N. Zeng, Y. Chen, X. Zhou, Generative adversarial networks and its applications in biomedical informatics, *Frontiers in Public Health*, 2020, **8**, 164, doi: 10.3389/fpubh.2020.00164.

[6] M. Khayatazad, L. De Pue, W. De Waele, Detection of corrosion on steel structures using automated image processing, *Developments in the Built Environment*, 2020, **3**, 100022, doi: 10.1016/j.dibe.2020.100022.

[7] F. B. Mansfeld, Corrosion mechanisms, Marcel Dekkar, New York, 1987, 165-209.

[8] M.-C. Zhao, M. Liu, G.-L. Song, A. Atrens, Influence of pH and chloride ion concentration on the corrosion of Mg alloy ZE41, *Corrosion Science*, 2008, **50**, 3168-3178, doi: 10.1016/j.corsci.2008.08.023.

[9] N. Pebere, C. Riera, F. Dabosi, Investigation of magnesium corrosion in aerated sodium sulfate solution by electrochemical impedance spectroscopy, *Electrochimica Acta*, 1990, **35**, 555-561, doi: 10.1016/0013-4686(90)87043-2.

[10] S. Mathieu, C. Rapin, J. Hazan, P. Steinmetz, Corrosion behaviour of high pressure Die-cast and semi-solid cast AZ91D alloys, *Corrosion Science*, 2002, **44**, 2737-2756, doi: 10.1016/s0010-938x(02)00075-6.

[11] F. Zucchi, V. Grassi, A. Frignani, C. Monticelli, G. Trabanelli, Electrochemical behaviour of a magnesium alloy containing rare earth elements, *Journal of Applied Electrochemistry*, 2006, **36**, 195-204, doi: 10.1007/s10800-005-9053-3.

[12] H. Ardelean, I. Frateur, P. Marcus, Corrosion protection of magnesium alloys by cerium, zirconium and niobium-based conversion coatings, *Corrosion Science*, 2008, **50**, 1907-1918, doi: 10.1016/j.corsci.2008.03.015.

[13] A. Frignani, V. Grassi, F. Zanotto, F. Zucchi, Inhibition of AZ31 Mg alloy corrosion by anionic surfactants, *Corrosion Science*, 2012, **63**, 29-39, doi: 10.1016/j.corsci.2012.05.012.

[14] H. Gao, Q. Li, Y. Dai, F. Luo, H. X. Zhang, High efficiency corrosion inhibitor 8-hydroxyquinoline and its synergistic effect with sodium dodecylbenzenesulphonate on AZ91D magnesium alloy, *Corrosion Science*, 2010, **52**, 1603-1609, doi: 10.1016/j.corsci.2010.01.033.

[15] W. Yang, Z. Liu, H. Huang, Galvanic corrosion behavior between AZ91D magnesium alloy and copper in distilled water, *Corrosion Science*, 2021, **188**, 109562, doi: 10.1016/j.corsci.2021.109562.

[16] X. Xie, A Review of Recent Advances in Surface Defect Detection using Texture analysis Techniques, *Electronic Letters on Computer Vision and Image Analysis*, 2008, **7**, 1-22, doi: 10.5565/REV/ELCVIA.268.

[17] F. F. Feliciano, F. R. Leta, F. Benedicto Mainier, Texture digital analysis for corrosion monitoring, *Corrosion Science*, 2015, **93**, 138-147, doi: 10.1016/j.corsci.2015.01.017.

[18] G. Sun, Imaging and quantitative measurement of corrosion in painted automotive and aircraft structures, AIP Conference Proceedings. Montreal (Canada). AIP, 2000, doi: 10.1063/1.1306104.

[19] X. Zhang, J. Zou, K. He and J. Sun, Accelerating Very Deep Convolutional Networks for Classification and Detection, *IEEE Transactions on Pattern Analysis and Machine Intelligence*, 2016, **38**, 1943-1955, doi: 10.1109/TPAMI.2015.2502579.

[20] Simonyan, K., and A. Zisserman, Very Deep Convolutional Networks for Large-Scale Image Recognition, 3rd International Conference on Learning Representations (ICLR 2015), Computational and Biological Learning Society, 2015.

[21] J. Redmon, A. Farhadi, YOLOv3: An Incremental Improvement. Computer Science, arXiv: 1804.02767, 2018, http://arxiv.org/abs/1804.02767.

[22] K. O'Shea, R. Nash, An introduction to convolutional neural networks, atomic energy of canada limited, AECL,1993, **10966**, 1-51, doi: 10.48550/arXiv.1511.08458.

[23] N. Idusuyi, O. J. Samuel, T. T. Olugasa, O. O. Ajide, R. Abu, Corrosion modelling using convolutional neural networks: a brief

overview, *Journal of Bio- and Tribo-Corrosion*, 2022, **8**, 1-8, doi: 10.1007/s40735-022-00671-3.
[24] D. J. Atha, M. R. Jahanshahi, Evaluation of deep learning approaches based on convolutional neural networks for corrosion detection, *Structural Health Monitoring*, 2018, **17**, 1110-1128, doi: 10.1177/1475921717737051.
[25] A. Sanjay Kumar, S. Manoj Kumar, R. Kiran Kumar, Optimized deep learning framework for detecting pitting corrosion based on image segmentation, *International Journal of Performability Engineering*, 2021, **17**, 627, doi: 10.23940/ijpe.21.07.p7.627637.
[26] E. Mohammed Abdelkader, O. Moselhi, M. Marzouk, T. Zayed, Entropy-based automated method for detection and assessment of spalling severities in reinforced concrete bridges, *Journal of Performance of Constructed Facilities*, 2021, **35**, doi: 10.1061/(asce)cf.1943-5509.0001544.

